Wigner-crystal phases in bilayer quantum Hall systems

Subha Narasimhan and Tin-Lun Ho
Physics Department, The Ohio State University, Columbus, Ohio 43210
(Received 17 November 1994; revised manuscript received 18 May 1995)

Electrons in double-layer quantum-well systems behave like pseudospin $\frac{1}{2}$ particles where the up and down "spin" represent localized states in each of the layers. The magnetically induced Wigner-crystals in these systems are therefore crystals of these pseudospin $\frac{1}{2}$ particles. We have calculated the phase diagram of the bilayer Wigner-crystals using a variational scheme which explores a *continuum* of lattice and spin structure. Five stable crystal phases are found. For the given tunneling strength and layer separation, one typically encounters the following sequence of transitions as the filling factor is increased from zero (the same sequence also occurs if one increases the "effective" layer separation starting from zero, with the tunneling strength and filling factor held fixed): (I) (One-component) hexagonal structure → (II) centered rectangular structure → (III) centered square structure → (IV) centered rhombic structure → (V) staggered hexagonal structure. Crystal I is a ferromagnet in pseudospin space. All other crystals (II–V) have mixed ferromagnetic and antiferromagnetic orders, which are generated by layer tunneling and interlayer repulsion, respectively. The relative strength of these two magnetic orders vary continuously with external parameters (i.e., the ratio of layer separation to magnetic length, the tunneling gap to Coulomb interaction, etc). The lattice structures I, III, and V are "rigid" whereas II and IV are "soft," in the sense that the latter two vary with external parameters and the former three do not. Another important feature of the phase diagram is the existence a multicritical point and a critical end point, which allows all crystals (except V) to transform into one another continuously. While our findings are based on a variational calculation, one can conclude on physical grounds that the mixed ferromagnetic-antiferromagnetic order as well as the pseudospin-lattice coupling should be general features of most bilayer Wigner-crystals.

I. INTRODUCTION

Recent experiments[1] have shown that bilayer quantum-well systems in strong magnetic fields behave like quantum Hall systems with (pseudo-)spin 1/2, where the up and down pseudospins correspond to electron states residing in one or the other of the layers. The behavior of this quantum Hall system is demonstrated by the quantum Hall effect at filling factors $\nu = 1/2$ and $\nu = 1$, which corresponds to each layer being 1/4 filled and 1/2 filled, respectively.[1] Since even denominator quantum Hall fluids do not exist in fully spin polarized single-layer systems, these states can only result from the correlations between electrons in different layers.

One major difference between single-layer and bilayer systems is their energy scales. In the single-layer case, if one restricts to the lowest Landau level, the only remaining energy scale is the Coulomb interaction between electrons $e^2\sqrt{n}$, where n is the electron density. [n is related to the filling factor ν as $n = \nu/(2\pi\ell^2)$, where $\ell = (c\hbar/eB)^{1/2}$ is the magnetic length.] For bilayer systems, there are three energy scales: (a) the tunneling energy Δ between the layers (precise definition given later); (b) the interlayer Coulomb interaction e^2/D, where D is the separation between the layers and; (c) the intralayer Coulomb interaction $e^2\sqrt{n}$, where $n = \nu/(2\pi\ell^2)$ is the total electron density of *both* layers. Because of these energy scales, the system can fall into different physical regimes depending on their relative ratios. The important physical regimes are as follows:

(i) Two single-layer regime, $e^2\sqrt{n} \gg e^2/D, \Delta$.

(ii) Two-component (or correlation) regime, $e^2\sqrt{n} \sim e^2/D \gg \Delta$.

(iii) One-component regime, $e^2\sqrt{n} \sim e^2/D < \Delta$.

Regime (i) corresponds to the case of large layer spacing. In this case, the systems reduces to two weakly interacting single-layer systems. Regime (iii) corresponds to sufficiently small layer spacing, so that the effects of tunneling becomes important. In this case, the electrons lie in the "symmetric" state of the quantum well. The system reduces again to the single-layer case. Regime (ii) is very different. Despite the weakness of layer tunneling, electrons are strongly coupled to each other through the Coulomb interaction. The $\nu = 1/2$ and $\nu = 1$ quantum Hall states are found in this regime.[1] In particular, the $\nu = 1/m$ states (m odd) are believed to behave like quantum ferromagnets.[2] [By one and two component, we have in mind a pseudospin 1/2 representation of the electron wave function. We shall discuss this representation shortly.]

For single-layer systems, it is well known that the quantum Hall fluids eventually lose their stability at sufficiently low filling factors to the Wigner crystals, which are essentially products of electron Gaussians arranged on a lattice, properly antisymmetrized to satisfy the Pauli principle. The emergence of Wigner crystals at low fill-

ing is inevitable, as electron exchange has weakened so much, that the correlation energy of the fluid falls below the Madelung energy of the Wigner solid. In the past few years, many experiments (transport,[4,5] threshold field,[6] magnetophonon,[7] and luminescence[8]) have indicated the existence of crystalline characteristics at various filling factors, some are as high as around $\nu = 1/5$.[4,5] While there are questions as to whether the insulating states around $\nu = 1/5$ are Wigner crystals or other kinds of insulators,[9] the general view is that the insulating states at lower filling factors will be Wigner crystals.[10]

The reasons for the appearance of Wigner crystal mentioned above also apply to the bilayer case. However, because of the additional internal degrees of freedom, bilayer systems have a much greater variety of Wigner-crystal states. A limited version of this rich variety can be seen even without calculations, which we present schematically in Fig. 1. When the layers are far apart [i.e., regime (i)], the system becomes two single layers, each one has its own hexagonal Wigner crystal. To reduce interlayer repulsion, these two crystals will be "staggered" as in the usual hexagonal close pack (i.e., the lattice points of one lattice lies directly above the centers of the triangles of the other). As the layer spacing D is reduced, one enters regime (ii). In this regime, the staggered hexagonal structure in regime (i) cannot survive, because the large interlayer repulsion will push the electrons to fill up the "vacancies" in the staggered structure. The simplest staggered crystalline structure without vacancies is the staggered square lattice shown in Fig. 1, where the lattice sites of one lattice sit above the centers of the other. As D decreases further, one enters regime (iii). As mentioned before, the bilayer system reduces to the single-layer case. The crystal structure is, therefore, hexagonal.

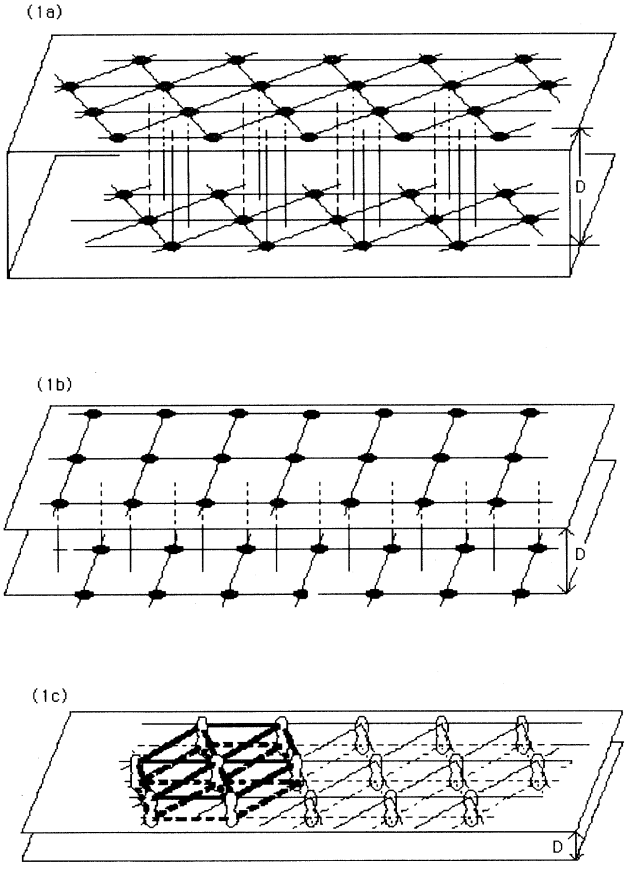

FIG. 1. (a) Staggered hexagonal structure in regime (i); (b) centered square structure in regime (ii); (c) single-component hexagonal structure in regime (iii). The electrons are in the symmetric state of the double quantum well, which are represented schematically by a "peanut" shape.

The purpose of this paper is to discuss how these crystals transform into one another as the energy parameters and the filling factors of the system are varied.[11] We have performed a variational calculation, which examines a large class of lattice and pseudospin structures. The resulting phase diagram is surprisingly rich. It contains more crystalline phases than the ones mentioned above. It also contains a multicritical point and a critical end point. A key feature of these crystal phases is that their spin structure vary over most parts of the phase diagram, even in those regions where the lattice structure remains fixed. In fact, as we shall see, the simple-minded staggered square structure mentioned above (which has fixed spin structure in the pseudospin language) is not the optimal structure in general. Another common feature is that all bilayer crystals acquire a net magnetization in the psuedospin space, except for the case of *strictly* zero tunneling. The existence of this magnetization has important implications on the macroscopic properties of these electron solids, which we shall discuss elsewhere.

The rest of this paper is organized as follows. In Sec. II, we describe our model and our variational wave function. The result of our calculation, i.e., the Wigner-crystal phase diagram, is presented in Sec. III. In Sec. IV, we describe in detail our calculational scheme. Although our variational scheme is conceptually straightforward, its actually implementation is not. The reason is that in evaluating the energy of a crystal structure, one has to evaluate many lattice sums, which are very slowly converging. Moreover, one has to repeat the energy calculation thousands of times in the minimization scheme. It is, therefore, necessary to develop tricks to speed up the evaluations of the lattice sums to the point that makes the minimization process feasible. When all the tricks are put together, the calculation is quite involved. To make the presentation as clear as possible, we first describe the computational strategy in detail in Sec. IV. The details of evaluating the relevant expressions are given in the Appendixes. At the end of Sec. IV, we also compare our results with the recent work of some others on the same subject. In Sec. V, we summarize our results, and emphasize those important features of bilayer Wigner crystals, which we believe should be model independent.

II. THE WIGNER CRYSTALS IN BILAYER QUANTUM HALL SYSTEMS

The model and the pseudospin representation. Consider the double-layer quantum well shown in Fig. 2. We shall adopt the coordinate system shown in Figs. 2(a) and (b). The origin of coordinate system is placed at the center of the well. The layers are parallel to the x-y plane. The position of an electron will be denoted as $\mathbf{x} = (\mathbf{r}, z)$, where $\mathbf{r} = (x, y)$ denotes a two-dimensional (2D) vector. We shall consider magnetic fields $\mathbf{H}$ normal the layers, i.e., along $\hat{\mathbf{z}}$. The Hamiltonian of a system with N electrons is $H = H_0 + V - B$, where H_0 is the single particle Hamiltonian, V is the electron-electron interaction, and B is the (divergent) classical contribution in V (which we shall define later). Explicitly, $H_0 = \sum_{i=1}^{N}[H_{||}(\mathbf{r}_i) + H_\perp(z_i)]$, where $H_{||}$ describes the cyclotron motion in the xy plane, and $H_\perp$ describes the motion along z,

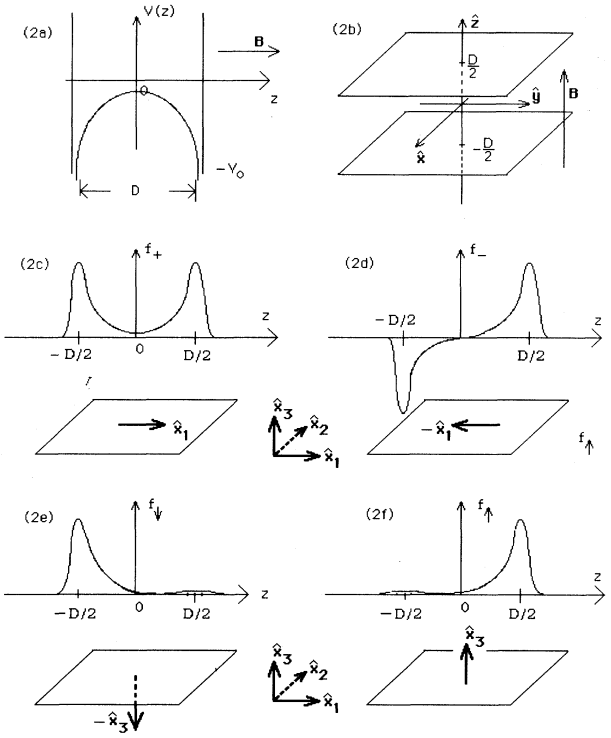

FIG. 2. A simple model of the double-layer quantum well and the pseudospin representation for the lowest doublet. The coordinate system and the quantum well potential are shown in (a) and (b). The ground state f_+ and the first excited state f_- are shown in (c) and (d). They are represented by spinors $\binom{1}{1}$ and $\binom{1}{-1}$, respectively, which have spin vectors along $+\hat{\mathbf{x}}_1$ and $-\hat{\mathbf{x}}_1$. (e) and (f) represent the sum and difference of these states, which are localized on the right and left well, respectively. These states are denoted as $f_\uparrow$ and $f_\downarrow$, and correspond to the spinors $\binom{1}{0}$ and $\binom{0}{1}$. The corresponding spin vectors are $\hat{\mathbf{x}}_3$ and $-\hat{\mathbf{x}}_3$.

$$H_{||}^0(\mathbf{r}) = \frac{1}{2m^*}\left(\frac{\hbar}{i}\frac{\partial}{\partial \mathbf{r}} - \frac{e}{2c}\mathbf{H}\times\mathbf{r}\right)^2, \qquad H_\perp(z) = -\frac{\hbar^2}{2m^*}\frac{d^2}{dz^2} + U(z), \tag{1}$$

m^* is the effective mass, and $U(z)$ is a double well potential, as shown in Fig. 2. We shall consider the case where the ground state and first excited state of $U(z)$ (denoted as f_+ and f_-, respectively) consist of maxima at $D/2$ and $-D/2$. (See Fig. 2.) The separation D between the maxima will be referred to as the "separation" between the layers.

The electron-electron interaction V is given by

$$V = \sum_{i>j}\frac{e^2}{|\mathbf{x}_i - \mathbf{x}_j|}. \tag{2}$$

Since the electrons are localized around $z = \pm D/2$, a system with total electron density n will contain a "classical" contribution B, which is the Coulomb energy of two infinitely thin layers located at $\pm D/2$, each with density $n/2$,

$$B = \frac{e^2}{2}\int d^3y d^3y' \frac{n_b(\mathbf{y})n_b(\mathbf{y}')}{|\mathbf{y}-\mathbf{y}'|}, \tag{3}$$

$$n_b(\mathbf{r}, z) = \frac{n}{2}\left[\delta(z - D/2) + \delta(z + D/2)\right]. \tag{4}$$

The ground state f_+ and the first excited state f_- are symmetric and antisymmetric about the center of the well. Their energies will be denoted by ϵ_+ and ϵ_-. For later discussions, we define

$$\Delta = \epsilon_- - \epsilon_+, \tag{5}$$

which we shall refer to as the "tunneling gap." The ground state of $H_{||}$ is the lowest Landau level with energy $\frac{1}{2}\hbar\omega_c$, $\omega_c = eH/m^*c$, with wave functions

$$u_m(\mathbf{r}) = \frac{([x+iy]/\ell)^m}{(2\pi 2^m m!\ell^2)^{1/2}} e^{-r^2/4\ell^2}. \tag{6}$$

For large magnetic fields and a sufficiently narrow well, it is sufficient to consider the lowest Landau level $\{u_m(x,y)\}$ and the "pseudospin 1/2" space spanned by f_+ and f_-. Although f_+ and f_- are eigenstates of $H_\perp$, sometimes it is more convenient to use the "localized" basis $f_\uparrow$ and $f_\downarrow$,

$$f_\uparrow = \frac{1}{\sqrt{2}}(f_+ + f_-), \qquad f_\downarrow = \frac{1}{\sqrt{2}}(f_+ - f_-), \tag{7}$$

which are states localized in the upper and lower layers, respectively (see Fig. 2). If we define spinors

$$f(z) = \begin{pmatrix} f_\uparrow(z) \\ f_\downarrow(z)\end{pmatrix}, \qquad \zeta = \begin{pmatrix}\zeta_\uparrow \\ \zeta_\downarrow\end{pmatrix}, \tag{8}$$

a general linear combination of f_+ and f_- can be written

as (using the fact that f is real)

$$f^\dagger \cdot \zeta \equiv \zeta_\uparrow f_\uparrow + \zeta_\downarrow f_\downarrow, \tag{9}$$

which is completely specified by the spinor ζ.

In defining the spinor f in Eq. (8), we have, in fact, implicitly chosen a coordinate system $(\hat{\mathbf{x}}_1, \hat{\mathbf{x}}_2, \hat{\mathbf{x}}_3)$ in the pseudospin space, so that $f_\uparrow$ and $f_\downarrow$ are eigenstates of $\sigma_3 = \vec{\sigma} \cdot \hat{\mathbf{x}}_3$, and f_+ and f_- are eigenstates of $\sigma_1 = \vec{\sigma} \cdot \hat{\mathbf{x}}_1$, respectively,

$$f_\uparrow \to \begin{pmatrix} 1 \\ 0 \end{pmatrix}, \qquad f_\downarrow \to \begin{pmatrix} 0 \\ 1 \end{pmatrix},$$
$$f_+ \to \frac{1}{\sqrt{2}} \begin{pmatrix} 1 \\ 1 \end{pmatrix}, \qquad f_- \to \frac{1}{\sqrt{2}} \begin{pmatrix} 1 \\ -1 \end{pmatrix}. \tag{10}$$

There are no relations between $(\hat{\mathbf{x}}_1, \hat{\mathbf{x}}_2, \hat{\mathbf{x}}_3)$ and the real space directions $\hat{\mathbf{x}}$, $\hat{\mathbf{y}}$, and $\hat{\mathbf{r}}_\perp$. In general, a spinor can be written as

$$\zeta = \begin{pmatrix} \cos\frac{\theta}{2} e^{-i\phi/2} \\ \sin\frac{\theta}{2} e^{i\phi/2} \end{pmatrix} e^{-i\chi/2}, \tag{11}$$

where θ and ϕ are the polar angles of its spin vector $\mathbf{S}$,

$$\mathbf{S} = \zeta^\dagger \vec{\sigma} \zeta = \cos\theta \hat{\mathbf{x}}_3 + \sin\theta \left(\cos\phi\ \hat{\mathbf{x}}_1 + \sin\phi\ \hat{\mathbf{x}}_2\right). \tag{12}$$

The spin vectors of f_+, f_-, $f_\uparrow$, and $f_\downarrow$ are $\hat{\mathbf{x}}_1$, $-\hat{\mathbf{x}}_1$, $\hat{\mathbf{x}}_3$, and $\hat{\mathbf{x}}_3$, respectively. (See Fig. 2.) In this representation, the energy of N noninteracting electrons in the lowest Landau level and in the pseudospin space is

$$H_0 = -\frac{1}{2}\Delta S_1, \qquad S_1 = \mathbf{S} \cdot \hat{\mathbf{x}}_1 = \sum_{i=1}^{N} S_{1,i}, \tag{13}$$

where we have ignored the constant $N(\hbar\omega_c/2)$.

Bilayer Wigner-crystal variational states: In the single-layer case, Wigner crystals can be constructed using coherent states.[12] A coherent state at $\mathbf{R}$ is defined as

$$\phi_{\mathbf{R}}(\mathbf{r}) = \frac{1}{\sqrt{2\pi\ell^2}} \exp\left(-\frac{r^2}{4\ell^2} + \frac{(x+iy)(R_x - iR_y)}{2\ell^2} - \frac{R^2}{4\ell^2}\right) \equiv \langle \mathbf{r}|\mathbf{R}\rangle. \tag{14}$$

A simple variational state for the Wigner crystal can be obtained by antisymmetrizing a product of coherent states distributed on a lattice $\{\mathbf{R}_i\}$. To simplify the notation, we write

$$\phi_{\mathbf{R}_i}(\mathbf{r}_j) \equiv \phi_i(j). \tag{15}$$

The Wigner-crystal wave function is then

$$|\Phi_{\rm wc}\rangle = \mathcal{A}\left[\prod_{i=1}^{N} |i\rangle\right] = \sum_P (-1)^P \left[\prod_{i=1}^{N} |Pi\rangle\right], \tag{16}$$

$$\Phi_{\rm wc}([\mathbf{r}]) = \mathcal{A}\left[\prod_{i=1}^{N} \phi_i(i)\right] = \sum_P (-1)^P \left[\prod_{i=1}^{N} \phi_{Pi}(i)\right], \tag{17}$$

where $[\mathbf{r}] \equiv (\mathbf{r}_1, \mathbf{r}_2, ..., \mathbf{r}_N)$, $\mathcal{A}$ is an antisymmetrizer for the electron coordinates $\{\mathbf{r}_j\}$, and P denotes a permutation of N objects with signature $(-1)^P$.

Bilayer coherent states are simply single-layer ones augmented by a pseudospin structure,

$$\phi_{\mathbf{R},\zeta}(\mathbf{x}) = (f^\dagger(z) \cdot \zeta)\phi_{\mathbf{R}}(\mathbf{r}) \equiv \langle \mathbf{x}|\mathbf{R}, \zeta\rangle, \tag{18}$$

recalling that $\mathbf{x} = (\mathbf{r}, z), \mathbf{r} = (x, y)$. The analog of the Wigner crystal of the single-layer case can be obtained by antisymmetrizing the product of a set of N coherent states, distributed on a regular array of N points $\{\mathbf{R}_i, i = 1, \ldots N\}$ in the x-y plane. Each point $\mathbf{R}_i$ is associated with a spinor $\zeta(\mathbf{R}_i)$ describing the wave function of this coherent state along $r_\perp$. As in the single-layer case, we write

$$\phi_i(\mathbf{j}) \equiv \phi_{\mathbf{R}_i,\zeta(\mathbf{R}_i)}(\mathbf{x}_j). \tag{19}$$

The index i now stands for both the 2D lattice site $\mathbf{R}_i$ and the spinor $\zeta(\mathbf{R}_i)$, where the boldface $\mathbf{j}$ denotes the three-dimensional coordinate $\mathbf{x}_j$ of the jth electron. In this notation, Wigner-crystal wave functions are still of the form Eq. (16). More explicitly, they are

$$\Phi_{\rm wc}([\mathbf{x}]) = \mathcal{A}\left[\prod_{i=1}^{N} \phi_i(\mathbf{i})\right] = \sum_P (-1)^P \left[\prod_{i=1}^{N} \phi_{Pi}(\mathbf{i})\right]. \tag{20}$$

Since these crystals are completely specified by the two-dimensional array $\{\mathbf{R}_i\}$ and the spinors $\{\zeta(\mathbf{R}_i)\}$, it is to useful to represent them as "two-dimensional" crystals of "spin 1/2" particles. In this representation, the hexagonal structure in regime (iii) [i.e., Fig. 1(c)] corresponds to the ferromagnetic state shown in Fig. 3(a), with magnetization along $\hat{\mathbf{x}}_1$, representing the symmetric state along $r_\perp$. The centered square [Fig. 1(b)] and staggered hexagonal [Fig. 1(c)] structures mentioned in Sec. I correspond to the antiferromagnetic structures shown in Figs. 3(b) and 3(c). The spins along $+\hat{\mathbf{x}}_3$ or $-\hat{\mathbf{x}}_3$ in these figures correspond to electrons in the upper or lower layer.

Ideally, one would like to do a variational calculation taking the set $\{\mathbf{R}_i\}$ and the spinors $\{\zeta(\mathbf{R}_i)\}$ as variables. Such a parameter space is too large to be practical. To anticipate the effects of tunneling on the lattice and the spin structure we have discussed, we restrict ourselves to the following configurations: We shall consider systems with an even number of electrons (N even). The array $\{\mathbf{R}_i\}$ consists of two lattices A and B, which are identical except shifted relative to one another by a vector $\mathbf{c}$. Spinors on the same lattice are identical, but need not be the same on different lattices. In other words, if $\mathbf{a}_1$ and $\mathbf{a}_2$ are basis vectors of A, then

$$\mathbf{R} = n_1\mathbf{a}_1 + n_2\mathbf{a}_2 \text{ and } \zeta(\mathbf{R}) = \zeta_A \text{ if } \mathbf{R} \in A,$$
$$\mathbf{R} = m_1\mathbf{a}_1 + m_2\mathbf{a}_2 + \mathbf{c} \text{ and } \zeta(\mathbf{R}) = \zeta_B \text{ if } \mathbf{R} \in B, \tag{21}$$

where $\{n_i, m_i\}$ are integers.

Our variational calculation is performed at fixed electron density n and fixed magnetic field. The variational parameters are the spinors ζ_A and ζ_B, the displacement vector $\mathbf{c}$, and the basis vectors $\mathbf{a}_1, \mathbf{a}_2$. The latter are subject to the constant area constraint $|\mathbf{a}_1 \times \mathbf{a}_2| = 2/n$. The energy function to be minimized is

$$E = \mathrm{Min}_{\Psi} \left(\frac{\langle \Psi | (V - B) | \Psi \rangle}{\langle \Psi | \Psi \rangle} - \Delta S_1 \right). \tag{22}$$

In the single-layer case, since there is only one energy scale, e^2/ℓ, the energy per particle is of the form

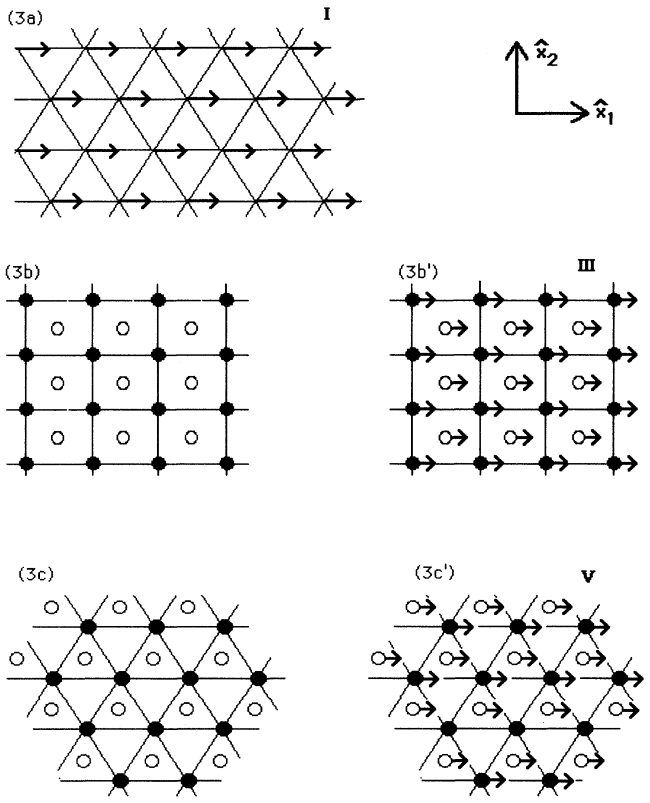

FIG. 3. The pseudospin representation of the crystals shown in Fig. 1. The one-component hexagonal crystal in Fig. 1(c) is represented by the ferromagnet hexagonal crystal in (a), with the magnetization along $\hat{\mathbf{x}}_1$. The centered square structure in Fig. 1(b) is represented by an antiferromagnet crystal in (b), with sublattice magnetization along $+\hat{\mathbf{x}}_3$ and $-\hat{\mathbf{x}}_3$, which are represented by solid and empty circles, respectively. This structure only exists at zero tunneling, $\Delta = 0$. When $\Delta \neq 0$, both up and down spins will tilt toward $\hat{\mathbf{x}}_1$ as shown in (b$\prime$). An arrow with a solid or (empty) circle attached to the base denotes a spin with positive (negative) $\hat{\mathbf{x}}_3$ component. The staggered hexagonal structure in (a) is represented by the antiferromagnetic structure in (c). Like (b), (c) only exists at zero tunneling. Nonzero tunneling will make the spins point along $\hat{\mathbf{x}}_1$ as shown in (c$\prime$). For later use, the structures in (a), (b$\prime$), and (c$\prime$) are denoted as I, II, and III, respectively. [See Figs. 4(a) to 4(c).]

$$\frac{E}{N} = \frac{e^2}{\ell} \mathcal{E}(\nu), \tag{23}$$

where $\mathcal{E}$ is a dimensionless function of ν. In the bilayer case, because of the three energy scales $e^2\sqrt{n}$, e^2/D, Δ, the energy per particle is of the form

$$E = \frac{e^2}{\ell} \mathcal{E}(D/\ell, \Delta/(e^2/\ell), \nu). \tag{24}$$

The labor of our calculation is to minimize the energy Eq. (22) within the variational space $\{\Gamma = (\zeta_A, \zeta_B, \mathbf{c}, \mathbf{a}_1, \mathbf{a}_2)\}$. The phase diagram of the system is given by the optimal configuration Γ^0, as a function of the experimental parameters $\{D/\ell, \Delta/(e^2/\ell), \nu\}$. In the next section, we shall present the Wigner-crystal phase diagram according to our calculation. The details of our calculation will be given in Sec. IV.

III. PHASE DIAGRAM

Our variational calculation reveals an unexpected Wigner-crystal phase diagram. Because of its richness, we shall display it in two different ways. We first show the phase diagram in the plane of $\Delta/(e^2/a)$ and D/a for various filling factors ν [see Figs. 4(a), 4(b), and 4(c)], where

$$a^2 = 2/n = 4\pi/\nu \tag{25}$$

is the area of the unit cell of lattice A. Since the layer spacing D and the tunneling gap Δ are fixed in actual experiments, variations in $\Delta/(e^2/a)$ and D/a correspond to varying the electron density n (say, by varying the gate voltages). Figures 4(a), 4(b), and 4(c) are for $\nu = 1/3, 1/5$, and 0, respectively. Of course, at $\nu = 1/3$ and $1/5$, the system is a quantum Hall fluid. The reason that we still choose to display the Wigner-crystal phase diagram at these fillings is because it is essentially unchanged at nearby fillings, where the system is no longer a quantum Hall fluid. In fact, when plotted in terms of the variables $\Delta/(e^2/a)$ and D/a, the phase boundaries show only relatively small shifts over a large range of filling factors. On the other hand, if the phase diagram is displayed in terms of the variable $\overline{\Delta} \equiv \Delta/(e^2/\ell)$ and ν for different values of D/ℓ [Figs. 5(a) to 5(d)], the movements of the phase boundaries become much more pronounced. Figures 5(a)–5(d) will be useful for experiments where electron densities are fixed, so that variations in the magnetic field cause variations in $\overline{\Delta}$ and ν.

We have found altogether five stable Wigner-crystal states. We shall label them together with their region of stability as I, II, III, IV, V. Roughly speaking, the two single-layer regime [i.e., regime (i)] mentioned in Sec. I is contained in region V. The correlation regime (ii) is contained in region II, III, IV. The one-component regime (iii) is contained in region I. The optimal spin configuration turns out to be

$$\mathbf{S}_{A(B)} = \sin\theta\hat{\mathbf{x}}_1 + (-)\cos\theta\hat{\mathbf{x}}_3. \quad (26)$$

The spin structure of crystal I is ferromagnetic (i.e., $\theta = 90°, \mathbf{S}_A = \mathbf{S}_B = \hat{\mathbf{x}}_1$). All other crystals have mixed ferromagnetic and antiferromagnetic order, with $0 \leq \theta < 90°$. This system has a uniform magnetization $2\sin\theta\hat{\mathbf{x}}_1$ and a staggered magnetization $2\cos\theta\hat{\mathbf{x}}_3$. The pure antiferromagnetic case $\theta = 0$ only occurs at zero tunneling. The five classes of stable Wigner-crystals are as follows.

Region I: One-component ferromagnet hexagonal crystals. The lattices A and B of these crystals are staggered in such a way so that their union is a hexagonal lattice [$\mathbf{a}_1 \cdot \mathbf{a}_2 = 0$, $a_2/a_1 = \sqrt{3}$, $a_1^2\sqrt{3}/2 = 1/n$, $\mathbf{c} =$

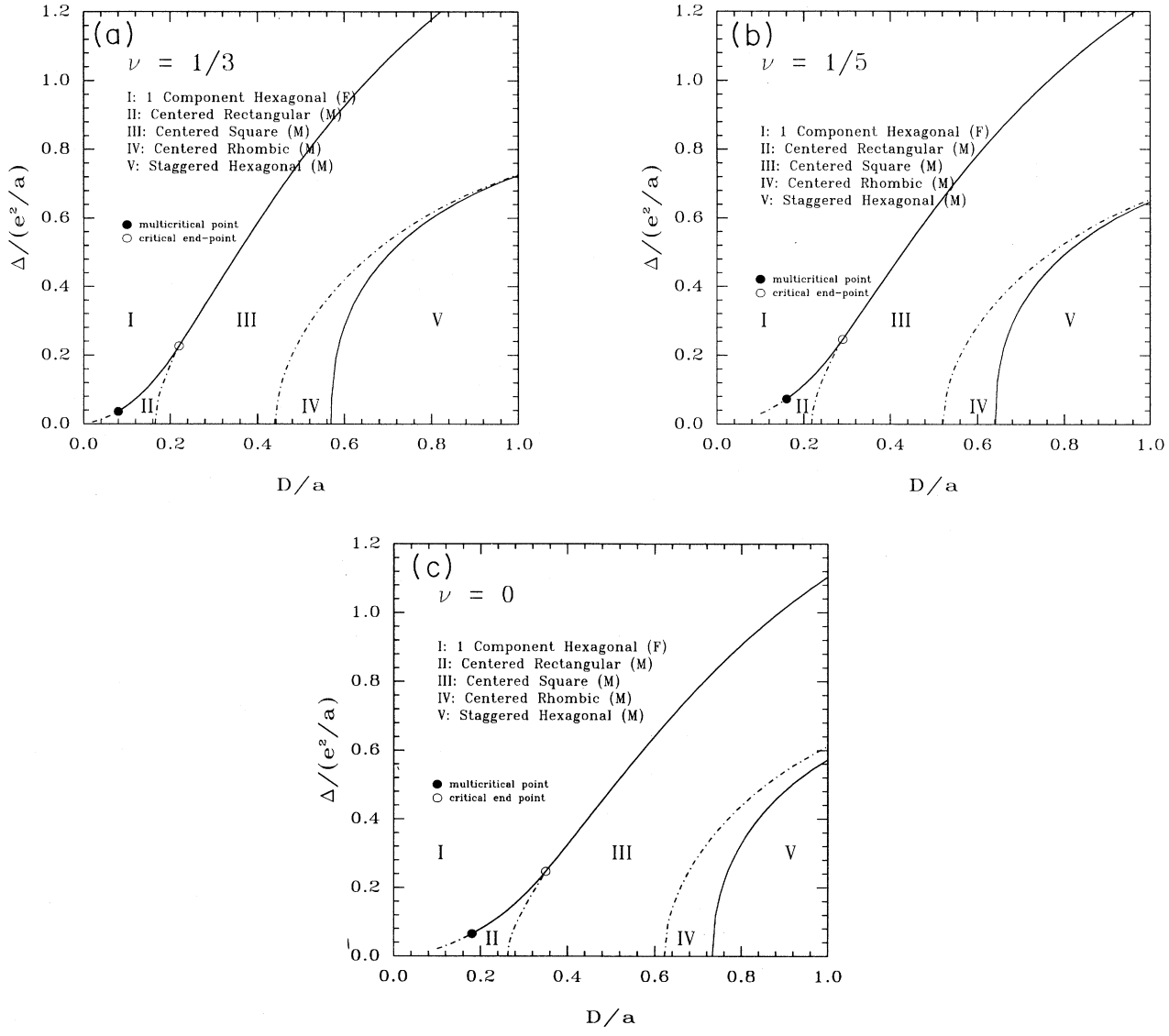

FIG. 4. (a), (b), and (c) show the Wigner-crystal phase diagram in the the plane of $\Delta/(e^2/a)$ and D/a, at filling factors $\nu = 1/3, 1/5$, and 0, where a^2 is the area of the unit cell in lattice A. Although the system is a quantum Hall fluid at these fillings, the Wigner-crystal phase diagram remains essentially the same at nearby fillings, where the system is no longer a quantum Hall fluid. The solid and dashed lines are first and second order lines, respectively. The label (F) means ferromagnetic order, (M) means mixed ferromagnetic and antiferromagnetic order. Both spin and lattice structure undergo discontinuous change across the first order line. The lattice structure in I, III, and V are "rigid," in the sense that they are unchanged in the entire I, III, and V region. In region II and IV, the lattice structure (i.e., $\mathbf{a}_1, \mathbf{a}_2$, and $\mathbf{c}$) varies with $\Delta/(e^2/a)$ and D/a. The spin structure is only "rigid" in region I, where it points along $\hat{\mathbf{x}}_1$. In all other regions, the spin angle varies with $\Delta/(e^2/a)$ and D/a. See Sec. III, for the determination of the spin angle θ.

$(\mathbf{a}_1 + \mathbf{a}_2)/2]$. In the entire region I, $\mathbf{S}_A = \mathbf{S}_B = \hat{\mathbf{x}}_1$, i.e., all electrons are in the symmetric state in the $r_\perp$ direction. This structure is "rigid." Both its lattice and spin structures are fixed in the entire region I.

Region II: Mixed ferromagnetic and antiferromagnetic centered rectangular crystals. Both sublattices A and B are rectangular lattices, with B sitting at the center of the unit cell of A: $[\mathbf{a}_1 \cdot \mathbf{a}_2 = 0,\ a_1 a_2 = 2/n,\ \mathbf{c} = (\mathbf{a}_1 + \mathbf{a}_2)/2]$. Unlike the "rigid" hexagonal structure in region I, these structures are "soft" in the sense that both the spin angle θ and the lattice parameter a_2/a_1 vary continuously throughout the entire region II [see Fig. 6(a)]. These crystals are separated from the hexagonal ones in region I by a first order line, which changes into a second order line at a multicritical point. It is also separated from crystal III mentioned below by a second order line, which intersects the I–II first order line at a critical end point.

Region III: Mixed ferromagnetic and antiferromagnetic centered square crystals. Both sublattices A and B are square lattices. They stagger in the same way as those in region II. The lattice structure of these crystals are rigid, with $[\mathbf{a}_1 \cdot \mathbf{a}_2 = 0, a_1 = a_2 = \sqrt{2/n}, \mathbf{c} = (\mathbf{a}_1 + \mathbf{a}_2)/2]$.

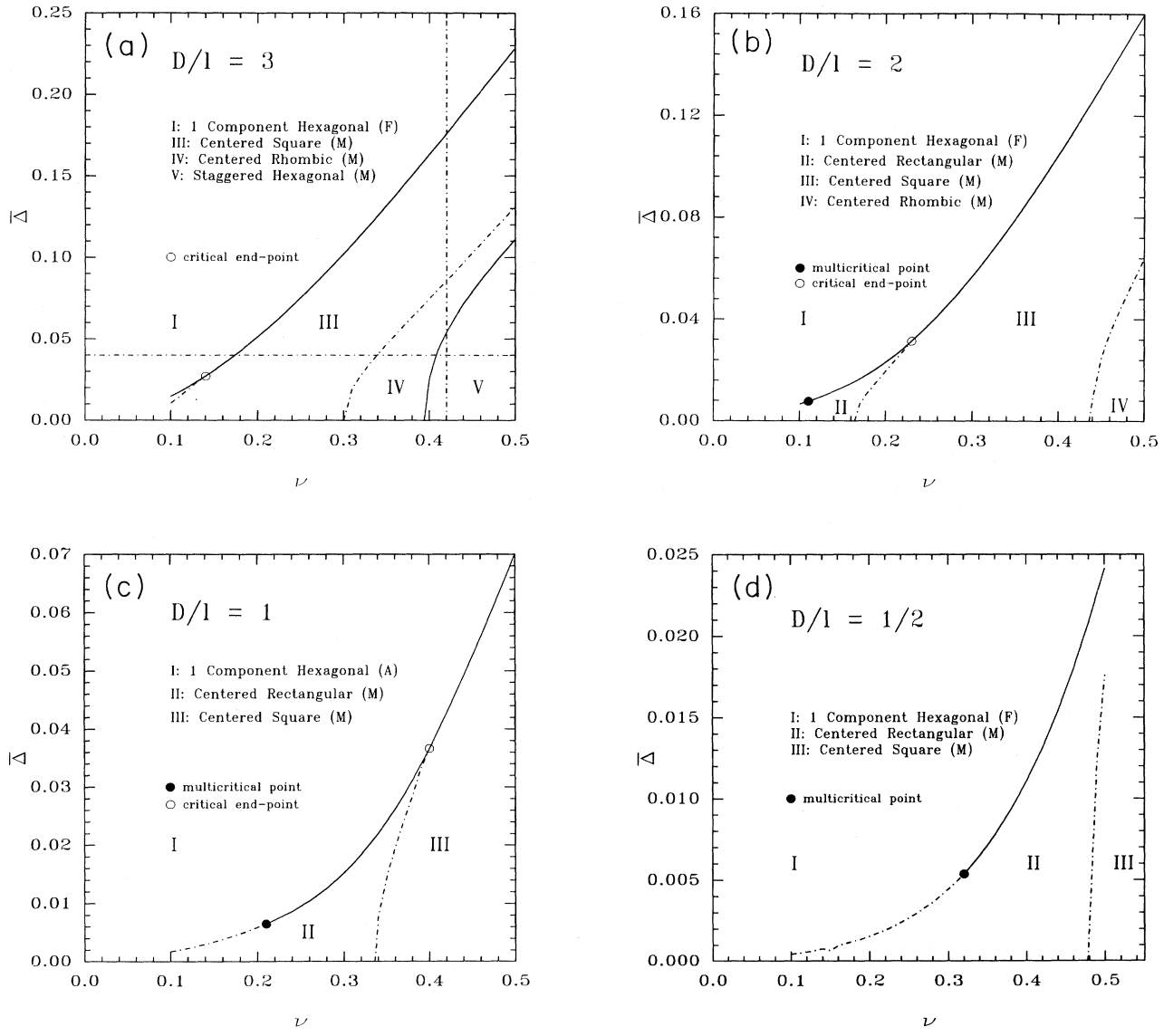

FIG. 5. (a) – (d) show the Wigner-crystal phase diagram as a function of $\overline{\Delta} \equiv \Delta/(e^2/\ell)$ and ν for $D/\ell = 3, 2, 1, 1/2$. When plotted in these variables, the phase boundaries show more changes when compared with those in Figs. 4(a)–4(c). In (a), both phase II and the multicritical point are not shown, for they appear at very small $\overline{\Delta}$ and ν. They are shown in (b), (c), and (d). The spin angle θ along the vertical and the horizontal line are shown in Figs. 7 and 8.

However, the spin structure is soft. The spin angle θ changes continuously within this region. These crystals are separated from crystal I by a first order line, and crystal II by a second order line.

Region IV: Mixed ferromagnetic and antiferromagnetic centered rhombic crystals. Both A and B are rhombic lattices. They stagger in the same way as crystal I and II. $[a_1 = a_2,\ a_1^2 \sin\alpha = 2/n, \mathbf{c} = (\mathbf{a}_1 + \mathbf{a}_2)/2]$. Like crystal II, this structure is soft. The spin angle θ, and the lattice angle α between $\mathbf{a}_1$ and $\mathbf{a}_2$ vary throughout the entire region IV [see Fig. 6(b)]. These crystals are separated from crystal III by a second order line, and crystal V mentioned below by a first order line.

Region V: Mixed ferromagnetic and antiferromagnetic staggered hexagonal crystals. Both A and B are hexagonal lattices. A is sitting above the center of triangle of B. The lattice structure is rigid, with $[a_1 = a_2,\ \alpha = 60°,\ a_1^2\sqrt{3}/2 = 2/n, \mathbf{c} = (\mathbf{a}_1 + \mathbf{a}_2)/3]$. However, its spin structure is soft. The angle θ varies over the entire region V.

Figures 7 and 8 show the variations of the spin angle along the horizontal and vertical line in Fig. 5(a). There is a large change in spin angle (about 20°) across the first order line separating the one-component hexagonal and centered square structure. However, the change across the centered rhombic and staggered hexagonal first order line is small (about 2°). As we shall explain in the next section, the spin angle for all cases is given by

$$\sin\theta = \begin{cases} 1 & \text{if } \gamma \le \overline{\Delta} \\ \overline{\Delta}/\gamma & \text{if } \gamma > \overline{\Delta}, \end{cases} \tag{27}$$

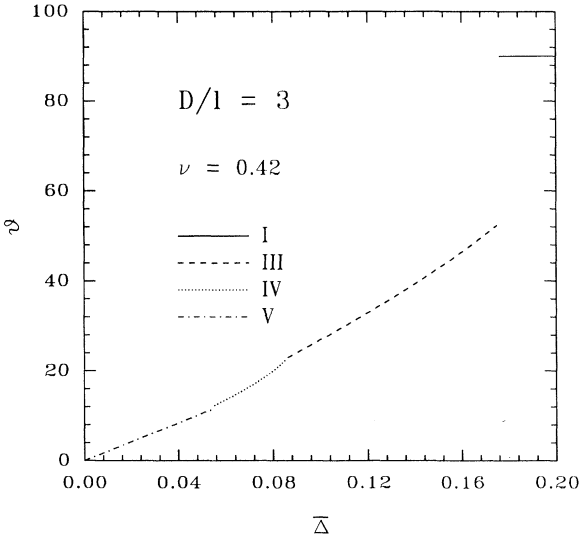

FIG. 7. The spin angle θ along the vertical line in Fig. 5(a). There is a close to 20° discontinuity across the I–III first order line, whereas there is a very small discontinuity (almost invisible on this scale) across the IV–V first order line.

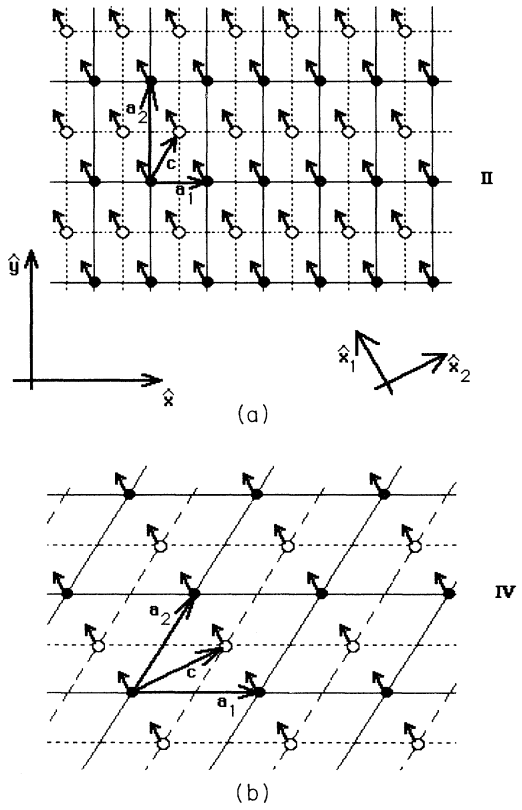

FIG. 6. (a) and (b) show the centered rectangular and centered rhombic structure (i.e., crystal II and IV) in Figs. 4(a)–4(c). The meaning of the arrows is identical to that in the caption of Fig. 3. The crystal (a) reduces to that in Fig. 3(a), when $a_2/a_1 = \sqrt{3}$, and $\theta = 90°$.

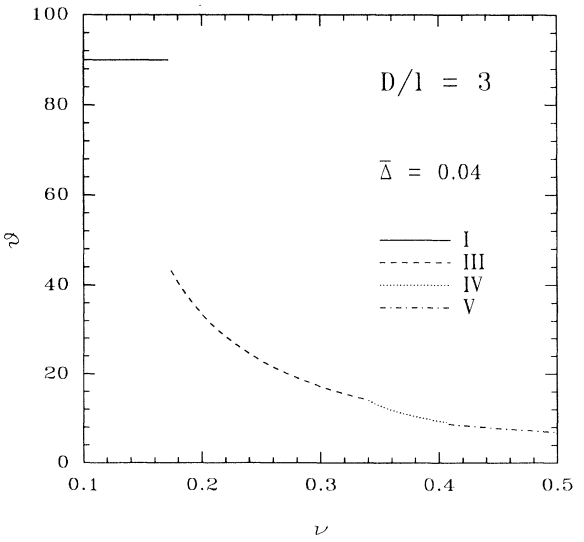

FIG. 8. The spin angle θ along the horizontal line in Fig. 5(a). The discontinuities of the spin angle across the I–III and IV–V first order lines are similar to that in Fig. 7.

where $\overline{\Delta} = \Delta/(e^2/\ell)$, and γ is a function of the lattice structure $(\mathbf{a}_1, \mathbf{a}_2, \mathbf{c})$, ν, and D/ℓ. For crystals I, III, V where the lattice structure is rigid (see descriptions I, III, V above), γ reduces to $\gamma^{\mathrm{I}}, \gamma^{\mathrm{III}}, \gamma^{\mathrm{V}}$ which are functions of ν and D/ℓ only. We have plotted these three curves in Figs. 9(a) – 9(d). Readers who are interested in the spin angle θ in regions I, III, V for given D/ℓ can extract their values from Eq. (27) using these curves. The determination of θ in regions II and IV is less straightforward, for the lattice structures are soft in these regions. One has to first determine the lattice structure by numerical minimization, and then evaluate γ following the prescriptions in Sec. IV and Appendixes C and D.

IV. VARIATIONAL CALCULATION

In this section, we shall describe in detail our variational calculation. Our goal is to minimize the energy per particle at fixed densities with respect to the variational Wigner-crystal wave functions of Eq. (20),

$$\mathcal{E} = \langle H \rangle / N = [\langle H_0 \rangle + \langle V \rangle - B] / N \equiv \mathcal{E}_0 + \mathcal{V} - \mathcal{B}, \quad (28)$$

where $\langle \hat{O} \rangle = \langle \Psi_{\mathrm{wc}} | \hat{O} | \Psi_{\mathrm{wc}} \rangle / \langle \Psi_{\mathrm{wc}} | \Psi_{\mathrm{wc}} \rangle$. To simplify the notation, we shall from now on measure lengths in units of magnetic length ℓ, and energy in units of e^2/ℓ. In these units, the tunneling energy is

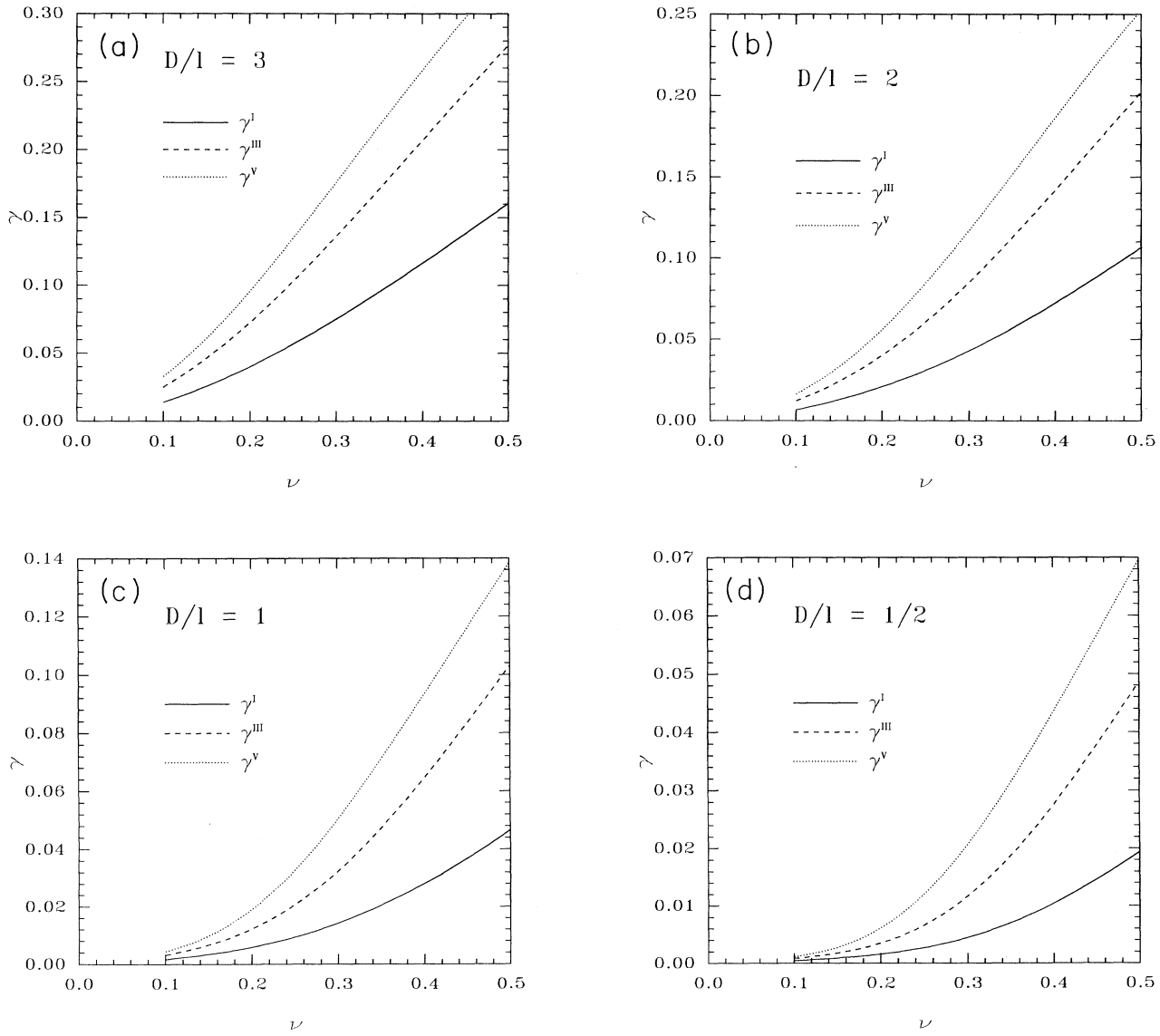

FIG. 9. (a) – (d) show $\gamma^{\mathrm{I}}, \gamma^{\mathrm{III}}, \gamma^{\mathrm{V}}$ as a function of ν for D/ℓ=3, 2, 1, 1/2. Using Eq. (48), these curves allow one to determine the spin angle θ for the crystals I, III, and V in Figs. 5(a) – 5(d).

$$\mathcal{E}_0 = -\frac{1}{4}\overline{\Delta}(S_1^A + S_1^B), \qquad \overline{\Delta} \equiv \Delta/(e^2/\ell). \tag{29}$$

Separating the background interaction $\langle B\rangle$ into contributions due to each layer, we have

$$\mathcal{B} = \frac{n}{4}\int \frac{d^2y}{y} + \frac{n}{4}\int \frac{d^2y}{\sqrt{y^2+D^2}} = -\left[\left.\frac{2\pi}{Ga^2}\right|_{G\to 0} - \frac{\pi D}{a^2}\right], \tag{30}$$

where $a^2 = 2/n = 4\pi/\nu$ is the unit cell area. Although bilayer Wigner crystals are more complex than the single-layer ones, they are identical in form when represented as in Eqs. (16) and (20). The evaluation of $\langle V\rangle$ can, therefore, proceed identically as in Maki and Zotos.[12] The result is an expansion in a set of n-body potentials,

$$\langle V\rangle = \sum_{i>j} V(ij) + \sum_{i>j>k} V(ijk) + \cdots, \tag{31}$$

where

$$V(ij) = \frac{(\langle ij| - \langle ji|)V(|ij\rangle - |ji\rangle)}{2(1-|\langle i|j\rangle|^2)}. \tag{32}$$

Recalling that i stands for $\mathbf{R}$ and $\zeta(\mathbf{R})$, we have

$$V(ij) = \frac{1}{2}\left(\frac{1}{1-|S(ij)|^2}\right)\int d^3x \int d^3x' \, \frac{1}{|\mathbf{x}-\mathbf{x}'|} \times|\phi_i(\mathbf{x})\phi_j(\mathbf{x}') - \phi_j(\mathbf{x})\phi_i(\mathbf{x}')|^2,$$
$$|S_{ij}|^2 = \left|\int d^3\mathbf{x}\, \phi_i^*(\mathbf{x})\phi_j(\mathbf{x})\right|^2. \tag{33}$$

The integrals in Eq. (33) include both direct and exchange terms, which are proportional to $|\phi_i(\mathbf{x})\phi_j(\mathbf{x}')|^2$ and $\phi_i^*(\mathbf{x})\phi_j(\mathbf{x})\phi_j^*(\mathbf{x}')\phi_i(\mathbf{x}')$, respectively. As in the single-layer case, the exchange terms as well as the n-body term for $n \le 3$ are smaller than the direct terms by a factor of $\exp[-R^2/2\ell^2]$, where $R = |\mathbf{R}_i - \mathbf{R}_j|$ is the distance between two coherent states. This factor is less than 10^{-3} for $\nu < 1/2$. Thus, if we focus on Wigner crystals at filling factors less than $1/2$, the exchange terms in Eq. (33) and the n-body terms in Eq. (31) for $n \le 3$ can be neglected. $V(ij)$ then takes the Hartree form,

$$V(ij) = \int d^3\mathbf{x} \int d^3\mathbf{x}' \frac{1}{|\mathbf{x}-\mathbf{x}'|}|\phi_i(\mathbf{x})\phi_j(\mathbf{x}')|^2 \qquad \text{for} \quad \nu < 1/2. \tag{34}$$

Next, using

$$\frac{1}{|\mathbf{x}-\mathbf{x}'|} = \int \frac{d^2q}{(2\pi)^2}\frac{2\pi}{q} e^{i\mathbf{q}\cdot(\mathbf{r}-\mathbf{r}')} e^{-q|r_\perp - r'_\perp|}, \tag{35}$$

Eq. (34) can be written as

$$V(ij) = \int_0^\infty dq\, e^{-q^2} J_0(qR) W(q), \tag{36}$$

$$W(q) = \int dudu'\, e^{-q|u-u'|}\, |f^\dagger(u)\cdot\zeta(\mathbf{R}_i)|^2 \times|f^\dagger(u')\cdot\zeta(\mathbf{R}_j)|^2. \tag{37}$$

Recall that $f_\uparrow(r_\perp)$ and $f_\downarrow(r_\perp)$ are localized around $r_\perp = D/2$ and $-D/2$. Typically, these functions decay away from the layers within a decay length $1/\kappa$ [i.e., $f_{\uparrow(\downarrow)}(r_\perp) \sim \exp(-\kappa|r_\perp - (+)D/2|)$]. In Appendix A, we show that as long as the products κD and $\kappa\ell$ are moderately larger than 1 (referred the "moderate" condition), the spinor products in Eq. (37) can be replaced by

$$|f^\dagger(u)\cdot\zeta|^2 = |\zeta_\uparrow|^2\delta(u - D/2) + |\zeta_\downarrow|^2\delta(u + D/2). \tag{38}$$

These "moderate" conditions are certainly feasible in experiments. Within the approximation Eq. (38), Eq. (36) reduces to the simple form

$$V(ij) = U_+(\mathbf{R}) + U_-(\mathbf{R})S_3(i)S_3(j) \equiv V_{S_3(i),S_3(j)}(\mathbf{R}), \tag{39}$$

$$U_\pm(\mathbf{R}) = \frac{1}{2}\int_0^\infty dq\, e^{-q^2}\,(1 \pm e^{-qD})\, J_0(qR), \tag{40}$$

where $\mathbf{R} = \mathbf{R}_i - \mathbf{R}_j$, $S_3(i) \equiv S_3(\mathbf{R}_i)$.

Note that the ineffectiveness of the exchange in Eqs. (33) and (37) does not mean that the problem is classical. Quantum mechanical effects are manifested through (a) the smearing of the (classical) δ-function density to a Gaussian in the lowest Landau level (thereby affecting the interaction of two electrons at distances of the order of ℓ), and (b) layer tunneling [i.e., the tunneling gap Δ in Eq. (29)]. [Note that the insignificance of layer exchange in Eq. (37) under the "moderate" condition does not mean that the tunneling gap in Eq. (29) can also be ignored. The reason is that Δ is of the order of $|\epsilon|e^{-\kappa D}$, $|\epsilon| = |\epsilon_+ + \epsilon_-|/2$. Even though $e^{-\kappa D}$ is small when κD is moderately larger than 1, Δ can still be comparable with with other energies in the system for sufficiently attractive quantum well, which makes ϵ sufficiently large.]

To evaluate $\mathcal{V}$, we separate the contributions from different lattices A and B. Denoting S_3^A and S_3^B as S and S', respectively, we have

$$\mathcal{V} = \frac{1}{4}\sum_{\mathbf{R}\neq 0}[V_{S,S}(\mathbf{R}) + V_{S',S'}(\mathbf{R})] + \frac{1}{2}\sum_{\mathbf{R}} V_{S,S'}(\mathbf{R}+\mathbf{c}) \tag{41}$$

$$\equiv \eta - \frac{\gamma}{4}\left(\frac{S_3^A - S_3^B}{2}\right)^2 + \frac{\lambda}{4}\left(\frac{S_3^A + S_3^B}{2}\right)^2, \tag{42}$$

$$\eta = \frac{1}{2}\left[\sum_{\mathbf{R}\neq 0} U_+(\mathbf{R}) + \sum_{\mathbf{R}} U_+(\mathbf{R}+\mathbf{c})\right], \tag{43}$$

$$\gamma = -2\left[\sum_{\mathbf{R}\neq 0} U_-(\mathbf{R}) - \sum_{\mathbf{R}} U_-(\mathbf{R}+\mathbf{c})\right], \tag{44}$$

$$\lambda = 2\left[\sum_{\mathbf{R}\neq 0} U_-(\mathbf{R}) + \sum_{\mathbf{R}} U_-(\mathbf{R}+\mathbf{c})\right]. \tag{45}$$

All the spin dependence in the energy are contained in Eq. (42) and Eq. (29), which contains (S_3^A, S_3^B) and $(S_1^A + S_1^B)$, respectively. Since both $\mathbf{S}^A$ and $\mathbf{S}^B$ are vectors of fixed length, it is easy to see that the energy is minimized when $S_2^A = S_2^B = 0$. Direct plotting shows that $U_-(R)$ is a positive, monotonic decreasing function of R. This means λ is strictly positive. γ may be positive or negative depending on whether $\mathbf{c}$ is smaller or larger than the shortest vector in A. In either case, it is straightforward to show that the optimum spin structure is

$$S_3^A = -S_3^B = \cos\theta, \qquad S_1^A = S_2^B = \sin\theta. \tag{46}$$

Thus, the total correlation energy per electron [Eq. (28)] is

$$\mathcal{E} = \xi + \frac{1}{4}\gamma\sin^2\theta - \frac{1}{2}\overline{\Delta}\sin\theta, \qquad \xi = \eta - \frac{1}{4}\gamma - \mathcal{B}. \tag{47}$$

The optimum spin angle is, therefore, given by

$$\sin\theta = \begin{cases} 1 & \text{if } \gamma \le \overline{\Delta} \\ \overline{\Delta}/\gamma & \text{if } \gamma > \overline{\Delta}, \end{cases} \tag{48}$$

and the corresponding energies are

$$\mathcal{E} = \begin{cases} \xi + \frac{1}{4}\gamma - \frac{1}{2}\overline{\Delta} & \text{if } \gamma \le \overline{\Delta} \\ \xi - \overline{\Delta}^2/(4\gamma) & \text{if } \gamma > \overline{\Delta}. \end{cases} \tag{49}$$

Thus, the determination of the correlation energy and the optimum spin structure for a given lattice reduces to the evaluation ξ and γ. To evaluate these quantities, it is useful to introduce the following sums. Let us define the functions

$$F_1(R) \equiv \int_0^\infty dq\; e^{-q^2} J_0(qR),$$
$$F_2(R) \equiv \int_0^\infty dq\; e^{-qD} e^{-q^2} J_0(qR), \tag{50}$$

and the lattice sums

$$Q_i = \sum_{\mathbf{R}\neq 0} F_i(|\mathbf{R}|), \quad \overline{Q}_i = \sum_{\mathbf{R}} F_i(|\mathbf{R}+\mathbf{c}|), \quad i = 1,2. \tag{51}$$

The functions η and γ (hence ξ and γ), can now be expressed as

$$\eta - \mathcal{B} = \frac{1}{4}\left[Q_1 + \overline{Q}_1 + Q_2 + \overline{Q}_2\right] - \mathcal{B}, \tag{52}$$
$$-\gamma = (Q_1 - \overline{Q}_1) - (Q_2 - \overline{Q}_2). \tag{53}$$

The evaluation of $\eta - \mathcal{B}$ and γ (or ξ and γ) reduces to the evaluation of the four sums $\{Q_i, \overline{Q}_i, i = 1,2\}$. The reason that we consider the particular combination $\eta - \mathcal{B}$ is because (as we shall see) each Q term has a divergent (classical) contribution, so that their total contribution is $\mathcal{B}$. As a result, the combination $\eta - \mathcal{B}$ is finite. Likewise, the differences $(Q_i - \overline{Q}_i), i = 1,2$ are all finite, because their divergent contributions cancel each other.

A straightforward forward evaluation of these sums proves highly impractical as they converge very slowly. On the other hand, an essentially exact evaluation is possible if one notes the following: (i) The asymptotic forms of $F_i(R), i = 1,2$ consist only of powers in $1/R$ or $1/\sqrt{R^2+D^2}$ (see Appendix B), (ii) all sums of the form $\sum_{\mathbf{R}\neq 0} R^{-(2n+1)}$ and $\sum_R 1/(R^2+D^2)^{n+1/2}$ (where n is a positive integer) can be either evaluated analytically or transformed into a rapidly convergent series convenient for numerical calculation. (See Appendix C.) We, therefore, adopt the following strategy.

(a) For any desired accuracy (which we choose to be 10^{-9}), we choose a cutoff Λ and a set of asymptotic functions $\{F_i^{\rm as}(R), i = 1,2\}$ which are obtained by retaining a few terms of the asymptotic expansions of $F_i(R)$, such that $\{F_i^{\rm as}(R)\}$ reduce to $\{F_i(R)\}$ within the desired accuracy for all $R > \Lambda$. (See Appendix B.) Next, we rewrite the lattice sums Q_i and $\overline{Q}_i$ as

$$Q_i = Q_i^{\rm sr} + Q_i^{\rm as}, \qquad \overline{Q}_i = \overline{Q}_i^{\rm sr} + \overline{Q}_i^{\rm as}, \tag{54}$$

where

$$Q_i^{\rm as} = \sum_{\mathbf{R}\neq 0} F_i^{\rm as}(R), \qquad \overline{Q}_i^{\rm as} = \sum_{\mathbf{R}} F_i^{\rm as}(|\mathbf{R}+\mathbf{c}|), \tag{55}$$

and

$$Q_i^{\rm sr} = \sum_{\mathbf{R}\neq 0} \left[F_i(R) - F_i^{\rm as}(R)\right]\Theta(\Lambda - R),$$
$$\overline{Q}_i^{\rm sr} = \sum_{\mathbf{R}} \left[F_i(|\mathbf{R}+\mathbf{c}|) - F_i^{\rm as}(|\mathbf{R}+\mathbf{c}|)\right]\Theta(\Lambda - R). \tag{56}$$

The superscipt sr means "short range," and $\Theta(x) = 1$ or 0 if $x >$ or < 0. It is clear that all the short range contributions $\{Q_i^{\rm sr}, \overline{Q}_i^{\rm sr}\}$ are finite.

(b) The sums $\{Q_i^{\rm as}, \overline{Q}_i^{\rm as}, i = 1,2\}$ are evaluated analytically by generalizing the method of Bonshall and Maradudin,[13] or transforming the sum into a very rapidly convergent series. These are done in detail in Appendixes C and D. As we shall see in Appendix C, all four asymptotic sums contain a divergent piece typical of Madelung sums. Separating out this divergent piece, they can all be written as

$$Q_1^{\rm as} = \frac{2\pi}{Ga^2}\Big|_{G\to 0} + T_1, \quad Q_2^{\rm as} = \frac{2\pi}{Ga^2}\Big|_{G\to 0} - \frac{2\pi D}{a^2} + T_2,$$
$$\overline{Q}_1^{\rm as} = \frac{2\pi}{Ga^2}\Big|_{G\to 0} + \overline{T}_1, \quad \overline{Q}_2^{\rm as} = \frac{2\pi}{Ga^2}\Big|_{G\to 0} - \frac{2\pi D}{a^2} + \overline{T}_2, \tag{57}$$

where the $\{T_i, \overline{T}_i\}$ are the finite parts of $\{Q_i^{\rm as}, \overline{Q}_i^{\rm as}\}$. Using Eqs. (52) and (53), ξ and γ in Eq. (47) are now expressed in terms of the finite quantities $\{T_i, \overline{T}_i, Q_i^{\rm sr}, \overline{Q}_i^{\rm sr}\}$:

$$\xi = (\eta - \mathcal{B}) - \frac{1}{4}\gamma,$$
$$\eta - \mathcal{B} = \sum_{i=1,2} \frac{1}{4}\left[Q_i^{\rm sr} + \overline{Q}_i^{\rm sr} + T_i + \overline{T}_i\right],$$
$$-\gamma = [(Q_1^{\rm sr} - \overline{Q}_1^{\rm sr}) - (Q_2^{\rm sr} - \overline{Q}_2^{\rm sr}) + (T_1 - \overline{T}_1) - (T_2 - \overline{T}_2)]. \tag{58}$$

The explicit expressions of T_i and $\overline{T}_i$ are given in Appendix C.

(c) The short range sums Q_1^{sr} and $\bar{Q}_1^{sr}$ can be evaluated directly. This is because the asymptotic function $F_1^{as}(R)$, is a simple sum of inverse powers of R, and $F_1(R)$ is proportional to the zeroth order Bessel function with imaginary argument, which is available in most math libraries. The evaluation of $\{Q_2^{sr}, \overline{Q}_2^{sr}\}$ is less straightforward as the integral $F_2(R)$ is not a tabulated special function. Although this function can be evaluated to high accuracy by numerical integration, incorporating this integration in the minimization process is too time consuming to be practical. However, this bottleneck can be eliminated by the following trick. We first evaluate $F_2(R)$ by numerical integration on a fine mesh within the short range region $R < \Lambda$. The values of $F_2(R)$ at any point not on the mesh can be obtained (to a desired accuracy) from the nearby mesh points by using the "cubic spline" interpolation.[14] This allows us to replace all necessary numerical integrations in our minimization process by the spline interpolates, which is enormously faster. With the short range contributions given by (c), and the asymptotic contributions given in Appendix C and D, our evaluation of the functions ξ and γ is complete.

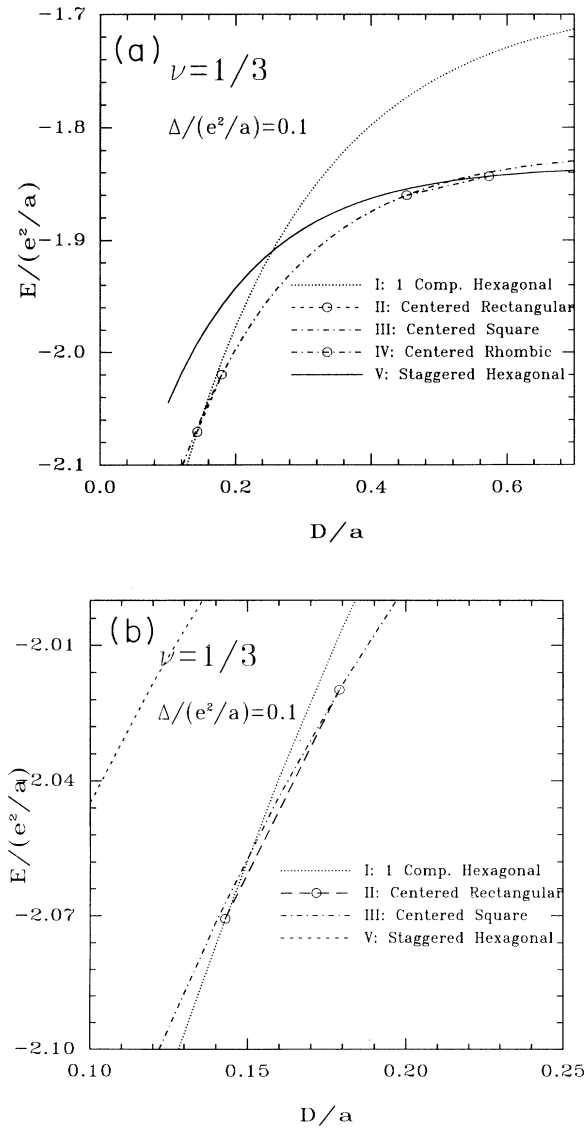

FIG. 10. (a) shows the energies of the crystal states I to V at $\nu = 1/3$ and $\Delta/(e^2/a) = 0.1$ as a function of layer separation D/a. (b) shows the transition region I–II and II–III in (a) on an expanded scale. The energy difference depicted is typically of the order of 10^{-3}.

The accuracy of the present calculation. The most serious approximation in our calculation is that the exchange terms are ignored in Eq. (33). As mentioned at the beginning of this section, the exchange terms are smaller than the direct terms by a factor of $e^{-R^2/2\ell^2}$, which is 10^{-3} around $\nu = 1/2$ and drops dramatically at lowering fillings (10^{-5} around $\nu = 1/3$ and 10^{-7} around $\nu = 1/5$). Once the exchange terms are dropped, the rest of our variational calculation is essentially exact. The numerical scheme that we have mentioned can easily achieve an accuracy of one part in 10^9 (and can be improved systematically). To demonstrate further the accuracy of our calculation, we show in Figs. 10(a) and 10(b) the energies of various crystal states at $\nu = 1/3$. The exchange energy is invisible on the scale of both figures. One can clearly see in Fig. 10 that the energy differences between different crystals range from 10^{-1} (far from the phase boundary) to 10^{-2} (close to the phase boundary), except for those between crystal I and II, and between II and III. The latter is shown on an expanded scale in Fig. 10(b), from which one can see that the energy difference of these crystals is typically of the order to 10^{-3}. Thus, the energy differences between all crystals are much greater than the exchanged energy 10^{-5}. Furthermore, the exchange energy appears as a *systematic correction* to all crystals. In comparing the energies between crystals of similar crystal structures, they are to a large extent cancelled out so that the actual exchange contributions to the energy *difference* are at least an order of magnitude smaller than 10^{-5}. The only place where our calculation may begin to produce a few percent error bar is close to $\nu = 1/2$. At lower fillings, all numerical evidence indicate that our evaluations of crystal energies are accurate to the order of $e^{-\pi/\nu}$ (which is the ratio between exchange and direct terms), and that the energy difference has an even higher accuracy ($10^{-1}e^{-\pi/\nu}$), because of the aforementioned systematic correction.

V. CONCLUDING REMARKS

We have seen that Wigner crystals in bilayer quantum Hall systems come in different "magnetic" and structural varieties. Among the crystal phases we have found that crystals I, III, and V occupy large areas of the parameter space, whereas crystals II and IV (especially II) occupy smaller regions. As we have seen in the previous paragraph, the energy differences between II and neigh-

boring crystals I and III are quite small ($\sim 0.1e^2/a$). It is, therefore, not clear whether they will survive Landau level mixing or will exist at finite temperature. Moreover, additional uncertainty can be added to the stability of II and IV, as the energy of the trial wave function can be improved by including correlation effects (such as those considered by Lam and Girvin and by Zhu and Louie[10]). It remains to be seen whether II and IV will be rescued or destroyed by these effects.

Despite the uncertainty of the fate of crystal II and IV, our results serve as a useful starting point for analyzing real data, as they provide a guide to look for various Wigner-crystal phases, and illustrate the richness of the bilayer crystal varieties. There are, however, two key features of the bilayer crystals revealed by our calculations that are immune to the factors mentioned in the previous paragraph (higher Landau level mixing, improvement of calculational scheme, etc). These features are direct consequences of the competition between layer tunneling and interlayer Coulomb repulsion and must exist in real systems. They are the coexistence of antiferromagnetic and ferromagnetic order, and the coupling between lattice and spin structure. The antiferromagnetism in pseudospin space is to minimize the interlayer Coulomb repulsion, whereas the ferromagnetism is to take advantage of the tunneling energy. The coupling between lattice and spin configurations simply reflects the competition of these two energies. In many ways, Wigner crystals in bilayer systems are like ^{3}He solids, which also have different phases with different lattice and magnetic structures. The magnetic structures in ^{3}He solids are known to give rise to many remarkable nuclear magnetic resonances. It will not be surprising if bilayer Wigner crystals also have many interesting "magnetic" properties.

ACKNOWLEDGMENTS

Part of this work was done during a three month's visit of T.L. Ho to the National High Magnetic Field Laboratory at Tallahassee, and at the Hong Kong University of Science and Technology. He would like to thank Nick Bonesteel and Bob Schrieffer for discussions, and specially C. Jayaprakash for discussions on multicritical points and critical end points. This work is supported in part by NHMFL through NSF Grant No. DMR 9016241.

APPENDIX A: CONDITIONS FOR EQ. (38)

The integrand in Eq. (37) contains terms like $f_\uparrow(u)^2 f_\downarrow(u')^2$, $f_\uparrow(u) f_\downarrow(u) f_\downarrow(u')^2$, $f_\uparrow(u)^2 f_\uparrow(u')^2$, etc. We shall discuss the contributions of the first two terms, from which the contributions of the rest can be similarly inferred. To simplify these expressions, we shift the origins of u and u', so that the maxima of $f_\uparrow$ and $f_\downarrow$ are at the origin,

$$f_\uparrow(u) = g(u - D/2) = f_\downarrow(-u). \tag{A1}$$

The contribution of $f_\uparrow(u)^2 f_\downarrow(u')^2$ and $f_\uparrow(u) f_\downarrow(u) f_\downarrow(u')^2$ to Eq. (37) can then be written as

$$I_1(q) = \int ds \int ds' e^{-q|D+s-s'|} g(s)^2 g(s')^2, \tag{A2}$$

$$I_2(q) = \int ds \int ds' e^{-q|D+s-s'|} g(s) g(s+D) g(s')^2. \tag{A3}$$

Since $g(s) \sim e^{-\kappa|s|}$, the exponential factor in Eqs. (A2) and (A3) can be replaced by $e^{-q(D+s-s')}$ if κD is moderately larger than 1. On the other hand, the Gaussian factor in Eq. (36) limits q to the range $q \leq 1/\ell$. Hence, if $\kappa\ell$ is moderately larger than one so that e^{-qs} decays much slower that $e^{-\kappa s}$, the functions $g(s)^2$ and $g(s')^2$ in Eq. (A2) will act like δ functions. The same approximations applies to I_2. However, because of the product, I_2 is smaller than I_1 by a factor of $e^{-\kappa D}$. It can, therefore, be ignored if κD is moderately larger than 1. Applying the analysis to other products of f's, we have Eq. (38).

APPENDIX B: ASYMPTOTIC EXPANSION OF $F_1(R)$ AND $F_2(R)$

Note that

$$F_1(R) = \int_0^\infty dq e^{-q^2} J_0(qR) = \frac{\sqrt{\pi}}{2} I_0^e(R^2/8), \tag{B1}$$

where $I_0^e(x) = e^{-x} I_0(x)$, and I_0 is the Bessel function with imaginary argument. For $R \gg 1$, F_1 has an asymptotic expansion

$$\begin{aligned} F_1(R) \to F_1^\infty(\mathbf{R}) &= \sum_{n=0}^\infty \frac{1}{n!} \nabla^{2n} \frac{1}{R} \\ &= \sum_{n=0}^\infty \frac{[(2n-1)!!]^2}{n!} \frac{1}{R^{2n+1}}. \end{aligned} \tag{B2}$$

For $R > \Lambda = 35$ (i.e., $\Lambda = 35\ell$ in the original unit), only three terms in the asymptotic series,

$$F_1^{\rm as}(R) = \left[1 + \nabla^2 + \frac{1}{2}\nabla^4\right] \frac{1}{R}, \tag{B3}$$

are enough to reproduce $F_1(R)$ to the accuracy of 10^{-9}.

In the case of $F_2(R)$, we note that it has the asymptotic expansion,

$$F_2(R) \to F_2^\infty(R) = \sum_{n=0}^\infty \left[\frac{(-1)^n}{n!} \frac{d^{2n}}{dD^{2n}}\right] \frac{1}{\sqrt{R^2+D^2}} \tag{B4}$$

$$= \sum_{n=0}^\infty (-1)^n \frac{(2n)!}{n!} \frac{1}{(R^2+D^2)^{n+1/2}} \times P_{2n}\left[\frac{D}{\sqrt{R^2+D^2}}\right]. \tag{B5}$$

$P_n(x)$ are the Legendre polynomials. As in the case of F_1, for $R > \Lambda = 35$, only three terms in the above series,

$$F_2^{\rm as}(R) = \left[1 - \frac{d^2}{dD^2} + \frac{1}{2}\frac{d^4}{dD^2}\right] \frac{1}{\sqrt{R^2+D^2}}, \qquad \text{(B6)}$$

are enough to reproduce $F_1(R)$ to the accuracy of 10^{-9}. $P_n(x)$ are the Legendre polynomials. The functions $F_1^{\rm as}(R)$ and $F_2^{\rm as}(R)$ are the asymptotic functions that we have used in our numerical calculation.

APPENDIX C: EXPLICIT DETERMINATION OF THE ASYMPTOTIC LATTICE SUMS $\{Q_i^{as}, \overline{Q}_i^{\rm as}, i = 1, 2\}$

Consider the following generating functions:

$$\begin{aligned} h(\mathbf{c}) &= \sum_{\mathbf{R}} \frac{1}{|\mathbf{R}+\mathbf{c}|}, \\ g(\mathbf{c}, D) &= \sum_{\mathbf{R}} \frac{1}{(|\mathbf{R}+\mathbf{c}|^2 + D^2)^{1/2}}, \end{aligned} \qquad \text{(C1)}$$

where $\mathbf{R} \in A$. Using the asymptotic functions $\{F_1^{\rm as}(R), F_2^{\rm as}(R)\}$ defined in Appendix B, it is easy to see that

$$\begin{aligned} Q_1^{\rm as} &= {\rm Lim}_{\mathbf{b}\to\mathbf{0}} \left[1 + \nabla_{\mathbf{b}}^2 + \frac{1}{2}\nabla_{\mathbf{b}}^4\right]\left(h(\mathbf{b}) - \frac{1}{b}\right), \\ \overline{Q}_1^{\rm as} &= \left[1 + \nabla_{\mathbf{c}}^2 + \frac{1}{2}\nabla_{\mathbf{c}}^4\right] h(\mathbf{c}), \\ Q_2^{\rm as} &= \left[1 - \frac{d^2}{dD^2} + \frac{1}{2}\frac{d^4}{dD^4}\right]\left(g(\mathbf{0}, D) - \frac{1}{D}\right), \\ \overline{Q}_2^{\rm as} &= \left[1 - \frac{d^2}{dD^2} + \frac{1}{2}\frac{d^4}{dD^4}\right] g(\mathbf{c}, D). \end{aligned} \qquad \text{(C2)}$$

We shall first give the expressions of h and g. Their derivations are given in Appendix D. These expressions are

$$\begin{aligned} h(\mathbf{c}) = {} & \frac{2\pi}{Ga^2}\bigg|_{G\to 0} + \frac{1}{a}[-2 + L(c/a)] \\ & + \frac{1}{a}\sum_{\mathbf{R}\neq 0}[L(|\mathbf{R}+\mathbf{c}|/a) \\ & + L(R/a)\cos(2\pi|\mathbf{R}\times\mathbf{c}|/a^2)], \end{aligned} \qquad \text{(C3)}$$

$$\begin{aligned} g(\mathbf{c}, D) = {} & \frac{2\pi}{Ga^2}\bigg|_{G\to 0} - \frac{2\pi D}{a^2} \\ & + \frac{1}{a}\left[\sum_{\mathbf{R}\neq 0} \frac{e^{-2\pi RD/a^2}}{(R/a)}\cos(2\pi|\mathbf{R}\times\mathbf{c}|/a^2)\right], \end{aligned} \qquad \text{(C4)}$$

where a^2 is the unit cell area of lattice A ($a^2 = 2/n = 4\pi\ell^2/\nu$) and

$$L(x) = \frac{1}{x}\left[1 - \phi(\sqrt{\pi}x)\right], \qquad \phi(y) = \frac{2}{\sqrt{\pi}}\int_0^y du\, e^{-u^2}. \qquad \text{(C5)}$$

The function ϕ is the error function.

It may seem that only Eq. (C4) is necessary because $h(\mathbf{c})$ is a limiting case of $g(\mathbf{c}, D)$. The latter is true but impractical. The reason is that the number of terms needed to be included in the sum in Eq. (C4) to achieve a specified accuracy grows as $1/D$ as $D \to 0$. The series in Eq. (C4) is, therefore, useless in the small D limit. We are, however, lucky for two reasons. First of all, the typical value of D in real experiments is of order unity. The series expansion Eq. (C4) is highly convergent for these D values. As for $h(\mathbf{c})$ [which corresponds to the special case $g(\mathbf{c}, D = 0)$], an analytic expression [Eq. (C3)] can be obtained by a straightforward generalization of the method of Bonshall-Maradudin (BM).[13] (See Appendix D.) This method produces a super convergent series for h (a cutoff of just four lattice constants in the sum is usually sufficient to produce an accuracy of 10^{-12}).

Next, we note that the gradients in Eq. (C2) can be conveniently evaluated using the following identities:

$$\begin{aligned} \nabla^2 L(r) \equiv L_2(r) &= \left[L(r) + p_1(\pi r^2)e^{-\pi r^2}\right]\Big/ r^2, \\ p_1(x) &= 4x + 2, \\ \nabla^4 L(r) \equiv L_4(r) &= \left[9L(r) + p_2(\pi r^2)e^{-\pi r^2}\right]\Big/ r^4, \\ p_2(x) &= 16x^3 - 8x^2 + 12x + 18. \end{aligned} \qquad \text{(C6)}$$

With these identities, using the definitions in Eq. (57), and Eq. (C2) it is straightforward to work out the finite parts $\{T_i, \overline{T}_i, i = 1, 2\}$ of the asymptotic sums $\{Q_i^{\rm as}, \overline{Q}_i^{\rm as}, i = 1, 2\}$. For $Q_1^{\rm as}$, we have

$$\begin{aligned} & {\rm Lim}_{\mathbf{b}\to\mathbf{0}}\left[h(\mathbf{b}) - 1/b\right] \equiv \frac{2\pi}{Ga^2}\bigg|_{G\to 0} + T_{1a}, \\ & {\rm Lim}_{\mathbf{b}\to\mathbf{0}}\nabla_{\mathbf{b}}^2\left[h(\mathbf{b}) - 1/b\right] \equiv T_{1b}, \\ & \frac{1}{2}{\rm Lim}_{\mathbf{b}\to\mathbf{0}}\nabla_{\mathbf{b}}^4\left[h(\mathbf{b}) - 1/b\right] \equiv T_{1c}, \\ & T_1 \equiv T_{1a} + T_{1b} + T_{1c}, \end{aligned} \qquad \text{(C7)}$$

where

$$\begin{aligned} T_{1a} &= \frac{1}{a}\left[-4 + 2\sum_{\mathbf{R}\neq\mathbf{0}} L(R/a)\right], \\ T_{1b} &= \frac{1}{a^3}\left[\frac{8\pi}{3} + \sum_{\mathbf{R}\neq\mathbf{0}}\left[L_2(R/a) - 4\pi^2(R/a)^2 L(R/a)\right]\right], \\ T_{1c} &= \frac{1}{2a^5}\left[-\frac{64\pi^2}{5} + \sum_{\mathbf{R}\neq\mathbf{0}}[L_4(R/a) \right. \\ & \qquad \left. + 16\pi^4(R/a)^4 L(R/a)]\right]. \end{aligned} \qquad \text{(C8)}$$

Similarly, for $\overline{Q}_1^{\rm as}$, we have

$$\begin{aligned} & h(\mathbf{c}) \equiv \frac{2\pi}{Ga^2}\bigg|_{G\to 0} + \overline{T}_{1a}, \qquad \nabla_{\mathbf{c}}^2 h(\mathbf{c}) \equiv \overline{T}_{1b}, \\ & \frac{1}{2}\nabla_{\mathbf{c}}^4 h(\mathbf{c}) \equiv \overline{T}_{1c}, \\ & \overline{T}_1 \equiv \overline{T}_{1a} + \overline{T}_{1b} + \overline{T}_{1c}, \end{aligned} \qquad \text{(C9)}$$

where

$$\overline{T}_{1a} = \frac{1}{a}\left[L(c/a) + \sum_{\mathbf{R}\neq 0}[L(|\mathbf{R}+\mathbf{c}|/a) + L(R/a)\cos(2\pi|\mathbf{R}\times\mathbf{c}|/a^2)]\right],$$

$$\overline{T}_{1b} = \frac{1}{a^3}\left[L_2(c/a) + \sum_{\mathbf{R}\neq 0}[L_2(|\mathbf{R}+\mathbf{c}|/a) - 4\pi^2(R/a)^2 L(R/a)\cos(2\pi|\mathbf{R}\times\mathbf{c}|/a^2)]\right],$$

$$\overline{T}_{1c} = \frac{1}{2a^5}\left[L_4(c/a) + \sum_{\mathbf{R}\neq 0}[L_4(|\mathbf{R}+\mathbf{c}|/a) + 16\pi^4(R/a)^4 L(R/a)\cos(2\pi|\mathbf{R}\times\mathbf{c}|/a^2)]\right]. \quad \text{(C10)}$$

Next, for $Q_2^{\rm as}$, we have

$$[g(\mathbf{0},D) - 1/D] \equiv \left(\frac{2\pi}{Ga^2}\bigg|_{G\to 0} - \frac{2\pi D}{a^2}\right) + T_{2a},$$
$$-\frac{d^2}{dD^2}[g(\mathbf{0},D) - 1/D] \equiv T_{2b},$$
$$\frac{1}{2}\frac{d^4}{dD^4}[g(\mathbf{0},D) - 1/D] \equiv T_{2c},$$
$$T_2 \equiv T_{2a} + T_{2b} + T_{2c}, \quad \text{(C11)}$$

where

$$T_{2a} = \frac{1}{a}\left[\frac{-1}{(D/a)} + \sum_{\mathbf{R}\leq 0}\frac{e^{-2\pi RD/a^2}}{R/a}\right],$$
$$T_{2b} = -\frac{1}{a^3}\left[-\frac{2!}{(D/a)^3} + \sum_{\mathbf{R}\neq 0} 4\pi^2(R/a)e^{-2\pi DR/a^2}\right],$$
$$T_{2c} = \frac{1}{2a^5}\left[-\frac{4!}{(D/a)^5} + \sum_{\mathbf{R}\neq 0} 16\pi^4(R/a)^3 e^{-2\pi DR/a^2}\right]. \quad \text{(C12)}$$

Finally, for $\overline{Q}_2^{\rm as}$, we have

$$g(\mathbf{c},D) \equiv \left(\frac{2\pi}{Ga^2}\bigg|_{G\to 0} - \frac{2\pi D}{a^2}\right) + \overline{T}_{2a},$$
$$-\frac{d^2}{dD^2}g(\mathbf{c},D) \equiv \overline{T}_{2b},$$
$$\frac{1}{2}\frac{d^4}{dD^4}g(\mathbf{c},D) \equiv \overline{T}_{2c},$$
$$\overline{T}_2 = \overline{T}_{2a} + \overline{T}_{2b} + \overline{T}_{2c}, \quad \text{(C13)}$$

where

$$\overline{T}_{2a} = \frac{1}{a}\sum_{\mathbf{R}\neq 0}\frac{e^{-2\pi RD/a^2}}{(R/a)}\cos(2\pi|\mathbf{R}\times\mathbf{c}|/a^2),$$
$$\overline{T}_{2b} = -\frac{1}{a^3}\sum_{\mathbf{R}\neq 0} 4\pi^2(R/a)e^{-2\pi DR/a^2}\cos(2\pi|\mathbf{R}\times\mathbf{c}|/a^2),$$
$$\overline{T}_{2c} = \frac{1}{2a^5}\sum_{\mathbf{R}\neq 0} 16\pi^4(R/a)^3 e^{-2\pi DR/a^2}\cos(2\pi|\mathbf{R}\times\mathbf{c}|/a^2). \quad \text{(C14)}$$

A final note—to obtain an overall accuracy in the correlation energy to eight significant digits, suitable cutoffs (Λ_h and Λ_g) for the lattice sums in Eqs. (C3) and (C4) are $\Lambda_h \approx 5a$ and $\Lambda_g \approx 20a^2/\pi D$ [so that $e^{-2\pi D\Lambda_h/a^2} \sim 10^{-11}$ in Eq. (C4)].

APPENDIX D: DERIVATION OF $h(c)$ AND $g(c,D)$

The series for $h(\mathbf{c})$ in Eq. (C3) can be derived by a straightforward generalization of the BM method.[13] We first write

$$h(\mathbf{c}) = \sum_{\mathbf{R}}\frac{2}{\sqrt{\pi}}\left(\int_0^w + \int_w^\infty\right)d\beta\, e^{-\beta^2|\mathbf{R}+\mathbf{c}|^2} \equiv (i) + (ii), \quad \text{(D1)}$$

where $w = \sqrt{\pi}/a$. After rescaling the integration variable, the second term (ii) can be written as

$$(ii) = \frac{1}{a}\sum_{\mathbf{R}} L(|\mathbf{R}+\mathbf{c}|/a), \quad \text{(D2)}$$

where $L(R)$ is defined in Eq. (C5). To evaluate the first term (i), we first convert the real space lattice sum into a sum in the reciprocal space [using the standard relation $\sum_{\mathbf{R}}\omega(\mathbf{R}) = \sum_{\mathbf{G}}\tilde{\omega}(\mathbf{G})/a^2$, where $\tilde{\omega}$ is the Fourier transform of ω],

$$(i) = \sum_{\mathbf{G}}\frac{2}{\sqrt{\pi}}\int_0^w d\beta\,\frac{\pi}{a^2\beta^2}e^{-G^2/4\beta^2 + i\mathbf{G}\cdot\mathbf{c}}. \quad \text{(D3)}$$

Changing $\beta \to w/\beta$, we have

$$(i) = \frac{2}{a}\sum_{\mathbf{G}}\int_1^\infty d\beta\, e^{-(G\beta/2w)^2 + i\mathbf{G}\cdot\mathbf{c}} \equiv \sum_{\mathbf{G}} I_{\mathbf{G}}. \quad \text{(D4)}$$

The $\mathbf{G} = 0$ term is connected to the $1/R$ divergence of the sum and has to be treated separately:

$$I_{\mathbf{G}=0} = \frac{2}{a}\mathrm{Lim}_{\mathbf{G}\to 0}\left[\int_0^\infty - \int_0^1\right]d\beta\, e^{-(G\beta/2w)^2 + i\mathbf{G}\cdot\mathbf{c}} = \frac{2\pi}{Ga^2}\bigg|_{G\to 0} - \frac{2}{a}. \quad \text{(D5)}$$

For the $\mathbf{G} \neq 0$ terms, we note that reciprocal lattice vectors $\mathbf{G}$ and real space lattice vectors $\mathbf{R}$ are related as $\mathbf{G} = 2\pi\hat{\mathbf{z}}\times\mathbf{R}/a^2$. We can then write

$$\sum_{\mathbf{G}\neq 0} I_{\mathbf{G}} = \frac{1}{a}\sum_{\mathbf{R}\neq 0} 2\int_1^\infty d\beta\, e^{-\pi R^2\beta^2/a^2 + i2\pi|\mathbf{R}\times\mathbf{c}|/a^2}$$
$$= \frac{1}{a}\sum_{\mathbf{R}\neq 0} L(R/a)\,\cos(2\pi|\mathbf{R}\times\mathbf{c}|/a^2). \quad \text{(D6)}$$

Substituting Eqs. (D2), (D5), and (D6) into Eq. (D1), we have Eq. (C3).

The derivation of Eq. (C4) for $g(\mathbf{c}, D)$ is as follows. We write $g(\mathbf{c}, D)$ as

$$g(\mathbf{c}, D) = \sum_{\mathbf{R}} \int \frac{d^2q}{(2\pi)^2}\frac{2\pi}{q}\, e^{i\mathbf{q}\cdot(\mathbf{R}+\mathbf{c})}\, e^{-qD}. \quad \text{(D7)}$$

Using the relation

$$\sum_{\mathbf{R}} e^{i\mathbf{q}\cdot\mathbf{R}} = \sum_{\mathbf{G}} (2\pi)^2\delta(\mathbf{q}-\mathbf{G})/a^2, \quad \text{(D8)}$$

we find

$$g(\mathbf{c}, D) = \sum_{\mathbf{G}} \frac{2\pi}{Ga^2} e^{i\mathbf{G}\cdot\mathbf{c} - GD}, \quad \text{(D9)}$$

which is Eq. (C4), if we treat the $\mathbf{G} = \mathbf{0}$ term separately, and write $\mathbf{G} = 2\pi\hat{\mathbf{z}}\times\mathbf{R}/a^2$.

[1] Y.W. Suen, L.W. Engel, M.B. Santos, M. Shayegan, and D.C. Tsui, Phys. Rev. Lett. **68**, 1379 (1992); J.P. Eisenstein, G.S. Boebinger, L.N. Pfeiffer, K.W. West, and Song He, *ibid.* **68**, 1383 (1992); S.Q. Murphy, J.P. Einstein, G.S. Boebinger, L.N. Pfeiffer, and K.W. West, *ibid.* **72**, 728 (1994); Y.W. Suen, H.C. Manoharan, X. Ying, M.B. Santos, and M. Shayegan, *ibid.* **72**, 3405 (1994).

[2] K. Yang, K. Moon, L. Zhang, A.H. MacDonald, S.M. Girvin, and S.C. Zhang, Phys. Rev. Lett. **72**, 732 (1994).

[3] T.L. Ho, Phys. Rev. Lett. **73**, 874 (1994).

[4] V.J. Goldman, M. Santos, M. Shayegan, and J.E. Cunningham, Phys. Rev. Lett. **65**, 2189 (1990). Also, see, M. Santos, Y. Suen, M. Shayegan, Y. Li, W. Engels, and D. Tsui, *ibid.* **68**, 1188 (1992).

[5] H.W. Jiang, R.L. Willett, H.L. Stormer, D.C. Tsui, L.N. Pfeiffer, and K.W. West, Phys. Rev. Lett. **65**, 663 (1990).

[6] Y.P. Li, T. Sajoto, L.W. Engel, D.C. Tsui, and M. Shayegan, Phys. Rev. Lett. **67**, 1630, (1991); F.I. Williams, P.A. Wright, R.G. Clark, E.Y. Andrei, G. Deville, D.C. Glattli, O. Probst, B. Etienne, C. Dorin, C.T. Foxon, and J.J. Harris, *ibid.* **66**, 3285 (1991).

[7] E.Y. Andrei, G. Deville, D.C. Glattli, F.I.B. Williams, E. Paris, and B. Etienne, Phys. Rev. Lett. **60**, 2765 (1988); F.I.B. Williams *et al.*, *ibid.* **66**, 3285 (1991).

[8] H. Buhmann, W. Joss, K. von Klitzing, I.V. Kukushkin, G. Martinez, A.S. Plaut, K. Ploog, and V.B. Timofeev, Phys. Rev. Lett. **65**, 1056 (1990).

[9] S. Kivelson, D.H. Lee, and S.C. Zhang, Phys. Rev. B **46**, 2223 (1992).

[10] R. Lam and S. Girvin, Phys. Rev. B **30**, 473 (1984); X. Zhu and S. Louie, Phys. Rev. Lett. **70**, 335 (1993); R. Price, P. Platzman, and S. He, *ibid.* **70**, 339 (1993).

[11] Wigner-crystal states in bilayer systems have recently been studied by a number of authors using Hartree-Fock methods [X. Chen and J. Quinn, Phys. Rev. B **45**, 11 054 (1992); R. Cote, L. Brey, and A. MacDonald, *ibid.* **46**, 10 239 (1992)]. Our work uses the variational method. It allows us to explore a much wider region in spin space and map out the phase diagram for a great range of parameters.

[12] K. Maki and Zotos, Phys. Rev. B **28**, 4349 (1983).

[13] L. Bonshall and A. Maradudin, Phys. Rev. B **15**, 1959 (1977).

[14] See, for example, W.H. Press, B.P. Flannery, S.A. Teukolsky, and W.T. Vetterling, *Numerical Recipes* (Cambridge University Press, Cambridge, England, 1986).